Journal of Materials Chemistry A

ROYAL SOCIETY OF CHEMISTRY

PAPER

View Article Online
View Journal | View Issue

Cite this: *J. Mater. Chem. A*, 2021, **9**, 6861

Fe ultra-small particles anchored on carbon aerogels to enhance the oxygen reduction reaction in Zn-air batteries†

Jinjin Shi,[a] Xinxin Shu,[b] Chensheng Xiang,[c] Hong Li,[a] Yang Li,[a] Wei Du,[d] Pengfei An,*[e] He Tian,*[c] Jintao Zhang*[b] and Haibing Xia*[a]

In this work, ultra-small Fe particles (Fe-UPs) anchored on carbon aerogel (CA) (Fe-UP/CA catalysts) are successfully prepared by the optimal pyrolysis of hollow composite particles of zeolitic imidazolate framework-8 (ZIF) coated with coordination complexes of tannic acid (TA) and Fe precursors. Within these Fe-UPs, each Fe–N_4 moiety is separated by one O atom while each Fe atom is coordinated with four N atoms and one O atom. The as-prepared Fe-UPs composed of the Fe–N_4–O–Fe–N_4 moiety ($Fe_{Fe-O-Fe}$-UPs) are proposed as a new type of active species for the first time, to the best of our knowledge. Moreover, different types of active species (such as Fe single atoms, $Fe_{Fe-O-Fe}$-UPs, and Fe nanoparticles) in the CA can be controlled by rationally adjusting the Fe-to-TA molar ratios. More importantly, $Fe_{Fe-O-Fe}$-UPs in Fe-UP/CA catalysts are realized at an Fe-to-TA molar ratio of 2.2. With the merits of both Fe-single atom and traditional Fe-NPs, the as-prepared $Fe_{Fe-O-Fe}$-UP/CA catalysts are able to regulate properly the adsorption of reactants and the desorption of intermediates and products due to their increasing size and the presence of the multi-metal-atom structure. Accordingly, the as-prepared $Fe_{Fe-O-Fe}$-UP/CA catalysts towards the oxygen reduction reaction (ORR) exhibit a higher half-wave potential (0.93 V *vs.* 0.89 V of Pt/C), a higher onset potential (1.08 V *vs.* 1.0 V of Pt/C), a higher kinetic current density (14.2 mA cm^{-2} at 0.9 V) and better long-term stability in alkaline media. Additionally, Zn-air batteries assembled with such electrocatalysts also exhibit a higher power density of 140.1 mW cm^{-2} and a larger specific capacity of 781.7 mA h g^{-1}, which are better than those of the state-of-the-art the commercial Pt/C catalyst.

Received 3rd January 2021
Accepted 5th February 2021

DOI: 10.1039/d1ta00031d

rsc.li/materials-a

Introduction

The performance of electrochemical devices for energy conversion and storage, such as fuel cells and Zn-air batteries, depends to a great extent on the kinetics of the oxygen reduction reaction (ORR) at the cathode.[1–3] However, their development has been seriously restricted by the sluggish kinetics of the ORR at the cathode as well as the high cost of platinum group metal (PGM)-based catalysts in the practical electrochemical devices.[4–7] Therefore, catalysts with M-N/C-based active sites towards the ORR have been widely investigated and are expected to replace PGM-based catalysts.[8–18] In addition, it is found that catalysts with Fe–N_4/C-based active sites are deemed to have the optimal catalytic activity towards the ORR because of

[a]*State Key Laboratory of Crystal Materials, Shandong University, Jinan, 250100, P. R. China. E-mail: hbxia@sdu.edu.cn*

[b]*School of Chemistry and Chemical Engineering, Shandong University, Jinan, 250100, P. R China. E-mail: jtzhang@sdu.edu.cn*

[c]*Center of Electron Microscope, State Key Laboratory of Silicon Materials, School of Materials Science and Engineering, Zhejiang University, Hangzhou, 310027, P. R China. E-mail: hetian@zju.edu.cn*

[d]*School of Environment and Material Engineering, Yantai University, Yantai 264005, P. R. China*

[e]*Beijing Synchrotron Radiation Facility, Institute of High Energy Physics, Chinese Academy of Sciences, Beijing, 100049, P. R. China. E-mail: anpf@ihep.ac.cn*

† Electronic supplementary information (ESI) available: Additional TEM images of ZIF particles, ZIF particles after ultrasonication treatment, ZIF particles with TA-etching, and their corresponding TEM images after freeze-drying; TEM images of Fe-based catalysts, digital photograph of $Fe_{Fe-O-Fe}$-UP/CA catalysts, LSV curves of $Fe_{Fe-O-Fe}$-UP/CA catalysts prepared under different pyrolysis conditions, C_{ZIF-TA} catalysts, C_{ZIF-Fe} catalysts and Fe-NP/CA catalysts; XRD patterns of $Fe_{Fe-O-Fe}$-UP/CA catalysts before and after acid treatment, C_{ZIF-TA} catalysts and C_{ZIF-Fe} catalysts; HAADF-STEM element mappings of $Fe_{Fe-O-Fe}$-UP/CA catalysts after the acid leaching treatment, HR-TEM images of $Fe_{Fe-O-Fe}$-UP/CA catalysts and their size histogram; the distributions of mesoporous and macropore pore diameter of C_{ZIF} materials, C_{ZIF-TA} catalysts, Fe-SA/CA catalysts and $Fe_{Fe-O-Fe}$-UP/CA catalysts; comparison in the EXAFS spectra of $Fe_{Fe-O-Fe}$-UP/CA catalysts with other samples; models of the possible local atomic configuration around Fe atoms within carbon materials with increasing particle size; LSV curves at different rotation rates and the corresponding K–L plots of C_{ZIF-TA} catalysts, Fe-SA/CA catalysts and the commercial Pt/C catalyst; and data of Zn-air battery assembled by Fe-NP/CA catalysts. See DOI: 10.1039/d1ta00031d

its strong O_2 adsorption and a lower energy barrier to break the O=O bond.[19–21] However, the performance of catalysts with Fe–N_4/C-based active sites is still unsatisfactory, possibly due to their too strong adsorption ability to oxygen species,[22,23] which have a weak desorption ability of intermediates and the released products in the ORR process.

According to the well-known Sabatier principle, good catalysts should balance the adsorption rate of reactants and the desorption rate of the released products during the whole ORR process.[22,24,25] It has been widely accepted that the interactions of oxygen with Fe–N_4/C-based active sites in the traditional nanoparticle (NP)-based carbon catalysts are so strong while those in single-atom catalysts (SACs) are so weak.[26] In addition, the activity of Fe–N_4/C-based catalysts increases while their durability decreases with decreasing NP size.[27,28] In this regard, Fe–N_4/C-based catalysts with average sizes between SACs and traditional NP-based catalysts may combine their merits. For example, our group reported that Fe-single atom-nanoclusters distributed in carbon materials ($C_{PANI\text{-}TA\text{-}Fe}$ Fe-SA-NC catalysts) consisting of the Fe–N_4–O–O–Fe–N_4 moiety as active sites were prepared by controlled chelation between tannic acid (TA) molecules and Fe precursors.[29] The as-prepared Fe-SA-NC catalysts indeed realized the combination of the merits of SACs and traditional NP-based catalysts. Moreover, the formation of the Fe–N_4–O–O–Fe–N_4 moiety in our Fe-SA-NC catalysts further weakens the strong adsorption ability of Fe–N_4/C-based catalysts to oxygen species, due to the doping of highly electronegative heteroatoms (such as O) as an electronic structure modifier into the Fe–N_4/C structure.[30] More recently, the Xing group reported a new strategy to introduce axial bonded O into the Fe–N_4 moiety for the formation of Fe–O–Fe bridge bonds in the Fe–N_4–O–Fe–N_4 moiety as active sites. In addition, the activity of the Fe–N_4–O–Fe–N_4 moiety with O modifiers as active sites is 10 times higher than that of the normal Fe–N_4 as active sites.[31] Therefore, it is desirable to fabricate carbon materials with uniform distribution of 2–3 nm ultra-small particles consisting of the Fe–N_4–O–Fe–N_4 moiety ($Fe_{Fe-O-Fe}$-UPs), which may combine the merits of SACs and traditional NP-based catalysts.

Meanwhile, carbon materials with interconnected porosity, high surface area, high electrical conductivity and excellent mass transfer properties are also paramount for their performance in the ORR.[32–34] Obviously, carbon aerogels (CAs) will be one of the best candidates. Bearing these ideas in mind, Fe ultra-small particles consisting of the Fe–N_4–O–Fe–N_4 moiety anchored on CAs ($Fe_{Fe-O-Fe}$-UP/CA catalysts) may achieve a high ORR activity comparable to that of PGM-based catalysts.

Herein, we developed a new but effective method to fabricate $Fe_{Fe-O-Fe}$-UP/CA catalysts by the optimal pyrolysis of freeze-drying powders of hollow particles of zeolitic imidazolate framework-8 (ZIF) coated with complexes formed by tannic acid (TA) and Fe precursors by controlled chelation at the optimal ratio. Then, the morphology, composition, surface area and types of active sites of the as-prepared $Fe_{Fe-O-Fe}$-UP/CA catalysts were studied in detail. Next, their ORR performances were investigated in alkaline media. As expected, the as-prepared $Fe_{Fe-O-Fe}$-UP/CA catalysts exhibit an outstanding ORR activity and durability, which are better than those of carbon materials with Fe–SAs and Fe-NPs as well as the commercial Pt/C catalyst. Finally, the performances of a Zn-air battery assembled with the as-prepared $Fe_{Fe-O-Fe}$-UP/CA catalysts as the air cathodes were further tested in alkaline aqueous solution.

Experimental section

Materials

Zinc nitrate hexahydrate ($Zn(NO_3)_2 \cdot 6H_2O$, 99%), absolute methanol, tannic acid (TA, 98%+) and ferric ammonium citrate (FAC, Fe 20.5–22.5%) were purchased from Sinapharm Chemical Reagent Co. Ltd (Shanghai, China). 2-Methylimidazole (99%) was purchased from Macklin Biochemical Co. Ltd (Shanghai, China). All chemicals were used directly as received. All the glassware was washed with *aqua regia* (3 : 1 v/v HCl (37%)/HNO_3 (65%) solution) and then rinsed thoroughly with ultrapure water before use. (**Caution:** *Aqua regia* solutions are dangerous and should be used with extreme care; never store these solutions in closed containers) Ultrapure water from a Milli-Q system (18 MΩ cm, Millipore) was used in all our experiments.

Synthesis of zeolitic imidazolate framework-8 particles (ZIF particles)

The synthesis of 40 nm ZIF particles was performed by the reported method with slight modification.[35] Typically, a methanol solution (50 mL) containing 2-methylimidazole (19.85 mmol) was added into another methanol solution (50 mL) containing $Zn(NO_3)_2 \cdot 6H_2O$ (2.47 mmol). Then, the mixed solution was kept at room temperature for one hour under stirring. Next, 40 nm ZIF particles were collected by centrifuging and methanol washing several times. Finally, the resulting ZIF particles were dried in an oven at 60 °C and stored for further use.

Synthesis of hollow ZIF-TA particles

The methanol solution (25 mL) containing 40 nm ZIF particles (0.5 g) was first sonicated for 30 min to obtain the methanol dispersion of dispersed ZIF particles, followed by centrifugation to remove the supernatant and the collection of ZIF particles. Then, the resulting ZIF particles were redispersed in a methanol solution (25 mL). To obtain hollow ZIF-TA particles with an optimal shell thickness, different concentrations of TA molecules (0.3, 3, 4, 5, 6, 8, 10, 12, 15 and 20 g L^{-1}) were added into the methanol dispersion of ZIF particles for etching. After vigorous stirring of about 6 min, hollow ZIF-TA particles were obtained by centrifuging. Finally, the resulting hollow ZIF-TA particles were dried at 60 °C in an oven and stored for further use. In our case, the optimal concentration of TA molecules is 5 g L^{-1}.

Synthesis of $C_{ZIF\text{-}TA}$ catalysts

A ceramic boat containing the powder of hollow ZIF-TA particles was transferred into a tube furnace, which was pyrolyzed at 900 °C for 3 h with a heating rate of 10 °C min^{-1} under flowing Ar gas. After naturally cooling to room temperature, the catalysts were eventually obtained ($C_{ZIF\text{-}TA}$ catalysts).

Synthesis of $C_{ZIF\text{-}Fe}$ catalysts

FAC (18 mg) was added into an aqueous dispersion (6 mL) containing the ZIF particles (0.3 g) under stirring. ZIF-Fe particles were formed by stirring the above mixture for 24 h. The powder of ZIF-Fe particles was obtained by freeze-drying, followed by pyrolysis at 900 °C for 3 h at a heating rate of 10 °C min^{-1} under flowing Ar gas. Eventually, the catalysts were obtained after a further acid treatment ($C_{ZIF\text{-}Fe}$ catalysts).

Synthesis of $Fe_{Fe-O-Fe}$-UP/CA catalysts

FAC (18 mg) was added into an aqueous dispersion (6 mL) containing the resulting hollow ZIF-TA particles (0.3 g) under stirring. ZIF-TA-Fe particles were formed by stirring the above mixture for 24 h due to complexation between TA and Fe(III) ions in water. The powder of ZIF-TA-Fe particles was obtained by freeze-drying, followed by pyrolysis at 900 °C for 3 h at a heating rate of 10 °C min^{-1} under flowing Ar gas. Eventually, $Fe_{Fe-O-Fe}$-UP/CA catalysts were obtained after a further acid treatment.

Synthesis of Fe-SA/CA catalysts and Fe-NP/CA catalysts

The Fe-SA/CA catalysts and Fe-NP/CA catalysts were also prepared by the same procedure used for the synthesis of $Fe_{Fe-O-Fe}$-UP/CA catalysts except that the added amount of FAC was changed to 3 mg and 36 mg, respectively.

Results and discussion

Synthesis and characterization of $Fe_{Fe-O-Fe}$-UP/CA catalysts

Scheme 1 shows the detailed procedure for the synthesis of $Fe_{Fe-O-Fe}$-UP/CA catalysts. First, uniform ZIF particles with an average diameter of *ca.* 40 nm (ZIF particles) were prepared in a large quantity by using the classic method reported in the literature (Scheme 1a and Fig. S1, ESI†),[35] followed by their purification, ultrasonication process (Fig. S2, ESI†) and redispersion into methanol to obtain monodisperse ZIF particles for further use. Next, an appropriate amount of TA molecules was added to the methanol dispersion of monodisperse ZIF particles under vigorous stirring (Fig. S3, ESI†). After stirring of about 6 min, these solid ZIF particles can be etched into hollow ZIF particles covered with TA molecules (ZIF-TA particles) on their outer surfaces (Scheme 1b and Fig. S4b, ESI†), followed by the addition of an appropriate amount of the Fe precursor. Since Fe(III) ions can strongly coordinate with TA molecules, Fe(III) ions would be absorbed onto the outer surfaces of the resulting hollow ZIF particles (ZIF-TA-Fe particles) due to the presence of TA molecules (Scheme 1c and Fig. S4c, ESI†). Then, the powder of ZIF-TA-Fe particles was obtained by vacuum freeze-drying, in which agglomerates of hollow ZIF particles would be formed (Scheme 1d) and their hollow feature still remains (Fig. S4d, ESI†). In addition, the XRD pattern of ZIF-TA-Fe particles is rather similar to that of hollow ZIF-TA particles and hollow ZIF particles (Fig. S5, ESI†), indicating that Fe(III) ions indeed are absorbed onto the outer surfaces, instead of entering into the structure of ZIF particles. Thus, Fe(III) ions may be rather close due to the agglomerates of ZIF particles.

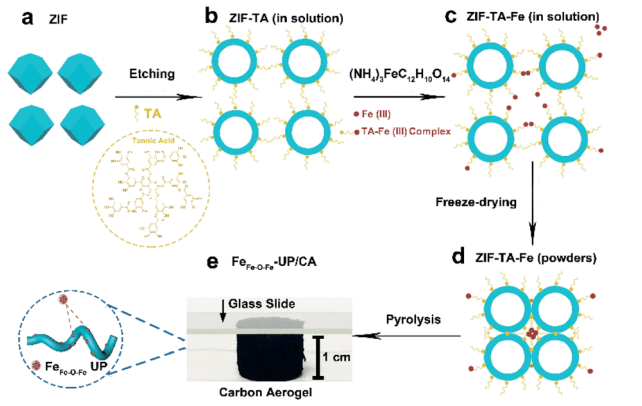

Scheme 1 Schematic illustration of the synthetic procedure of $Fe_{Fe-O-Fe}$-UP/CA. (a) Synthesis of ZIF particles in methanol, (b) formation of hollow ZIF-TA particles by TA etching in methanol, (c) formation of ZIF-TA-Fe particles by complexation between TA and Fe(III) ions in water, (d) powders of ZIF-TA-Fe particles after freeze-drying, and (e) transformation of powders of ZIF-TA-Fe particles into $Fe_{Fe-O-Fe}$-UP/CA by the pyrolysis process under the optimal conditions. Enlarged image is the schematic illustration of Fe-UPs anchored on carbon aerogels.

It is known that the presence of Fe species during the pyrolysis can lead to the *in situ* formation of carbon nanotubes (CNTs), and thus, the conductivity of the as-prepared carbon materials would be improved due to the increasing graphitization degree of carbon, which would be conducive to the rapid electron transfer during the ORR.[36] Accordingly, the powder of hollow ZIF particles containing an appropriate amount of Fe(III) ions is necessary to guarantee the formation of CAs with an optimal ratio of carbon nanotube-to-hollow carbon spheres and inlaid with high density Fe-UPs after the pyrolysis (Scheme 1e, Fig. S6 and S7b, ESI†), instead of the formation of Fe-single atoms on carbon aerogels (Fe-SA/CA) or Fe-NP/CA (Fe nanoparticles on carbon aerogels) (Fig. S7a and c, ESI†). Thus, the optimal ratio of TA-to-Fe(III) ions for synthesis of $Fe_{Fe-O-Fe}$-UP/CA catalysts is determined to be about 2.2. Finally, $Fe_{Fe-O-Fe}$-UP/CA catalysts were obtained (Scheme 1e and Fig. 1) by the pyrolysis process under the optimal conditions (Fig. S8, ESI†) and further acid leaching treatment. Note that after a series of control experiments, the pyrolysis temperature, holding time and heating rate are determined as 900 °C, 3 h and 10 °C min^{-1}, respectively (Fig. S8, ESI†). In addition, after further acid leaching treatment of 6 h, some big Fe NPs existing in the CAs can be totally removed, which are demonstrated by results of TEM images, EDS mapping, LSV curves and XRD patterns (Fig. S9–S11, ESI†). As such, the as-prepared $Fe_{Fe-O-Fe}$-UP/CA catalysts fabricated by the optimal pyrolysis by the synergism of TA and Fe precursors can have better electrocatalytic performance (Fig. S9c and S13a, ESI†), compared with the obtained carbon materials only with using Fe (Fig. S12a and S13b, ESI†) or TA precursors (Fig. S12b and S13c, ESI†). Note that Fe-UPs in $Fe_{Fe-O-Fe}$-UP/CA catalysts are composed of the $Fe-N_4-O-Fe-N_4$ moiety, instead of pure Fe atoms. Thus, Fe UPs after the 6 h acid-leaching treatment can be retained (Fig. S9a–c, ESI†). This result further indicates that Fe UPs in our case are different from pure Fe NPs, but similar to Fe SAs. These results are in

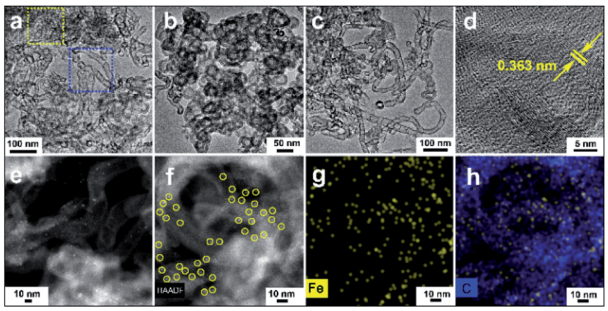

Fig. 1 Low (a) and high magnification (b and c) TEM images of $Fe_{Fe-O-Fe}$-UP/CA catalysts, high-resolution TEM image (d) of one part of the selected carbon nanotube in $Fe_{Fe-O-Fe}$-UP/CA catalysts, atomic resolution HAADF image (e) of $Fe_{Fe-O-Fe}$-UP/CA catalysts, and typical HAADF-STEM-EDS mapping images (f–h) of $Fe_{Fe-O-Fe}$-UP/CA catalysts. Note that (b) and (c) show enlarged images of areas within the yellow dotted box and the blue dotted box in (a), respectively.

good agreement with the EXAFS results (shown later). However, by extending the time for the acid leaching treatment to 8 h (Fig. S9d, ESI†), the Fe–N_4 moiety may be destructed to some degree based on their decreasing ORR performance (Fig. S10, ESI†).

As shown in Fig. 1a, the as-prepared $Fe_{Fe-O-Fe}$-UP/CA catalysts indeed exhibit a continuous porous 3D network structure, which is composed of inter-connected hollow carbon spheres (Fig. 1b) and entangled carbon nanotubes with a great number of bamboo-like joints (Fig. 1c). The presence of carbon nanotubes in CAs is expected to favor both mass and electron transfer during the catalytic reaction[37] although they will slightly lower the whole BET surface area, compared with CAs completely consisting of hollow carbon spheres. Moreover, a graphite-like layered structure with an interlayer spacing of 0.363 nm can be clearly observed in both carbon nanotubes (Fig. 1d) and hollow carbon spheres (Fig. S14a, ESI†) in the high-resolution TEM image of $Fe_{Fe-O-Fe}$-UP/CA catalysts, which can be attributed to the (002) plane of graphitic carbon,[38] indicating the high crystallization degree of the as-prepared CAs obtained by the pyrolysis treatment at the high temperature. Furthermore, on the basis of their EDS result, the as-prepared $Fe_{Fe-O-Fe}$-UP/CA catalysts are composed of elemental C (92.03 wt%), N (2.16 wt%), O (5.34 wt%) and Fe (0.46 wt%), and their distributions over the entire CAs are rather uniform (Fig. S15, ESI†). The total mass loading of elemental Fe in $Fe_{Fe-O-Fe}$-UP/CA catalysts is close to that in most of Fe-SA catalysts reported so far,[39] indicating that $Fe_{Fe-O-Fe}$-UP/CA may have high ORR activity as Fe–SA catalysts.

Because of the low contrast between Fe-UPs and CAs, there are no Fe-UPs observed in the TEM image (Fig. 1a to d). Thus, the atomic resolution high-angle annular dark-field (HAADF) image and HAADF-scanning transmission electron microscopy-energy dispersive spectroscopy (HAADF-STEM-EDS) mapping (Fig. 1e to h) were further used to demonstrate the formation of Fe-UPs in the as-prepared $Fe_{Fe-O-Fe}$-UP/CA catalysts. As shown in the HAADF images (Fig. 1e and S16, ESI†), plenty of bright dots with an average size of 3 nm are clearly observed. Moreover, in the HAADF-STEM-EDS mapping image (Fig. 1f–h), the profiles of distribution of elemental Fe (Fig. 1g) show a lot of ultra-small spherical spheres (yellow), which are rather consistent with the positions of the bright dots in Fig. 1f and h. Furthermore, the profiles of distribution of elemental Fe and elemental C in the overlapping image (Fig. 1h) are in good agreement with those in HAADF image (Fig. 1f). These results indicate that a high density of Fe-UPs are indeed formed and are anchored on the surfaces of CNTs in CAs.

The X-ray diffraction (XRD) pattern was further recorded to investigate the crystalline phase of carbon materials (Fig. 2a). There are no any diffraction peaks related to Zn observed in C_{ZIF} materials, $C_{ZIF\text{-}TA}$ catalysts, Fe-SA/CA catalysts and $Fe_{Fe-O-Fe}$-UP/CA catalysts, indicating the absence of elemental Zn. Compared with C_{ZIF} materials, $C_{ZIF\text{-}TA}$ catalysts, and Fe-SA/CA catalysts (Fig. 2a), one can clearly see that one relatively sharp peak located at 26.2° exists in the XRD pattern of $Fe_{Fe-O-Fe}$-UP/CA catalysts (Fig. 2a), which corresponds to the (002) planes of graphitic carbon,[40] indicative of the formation of highly graphitized carbon. Moreover, the typical peaks of metallic Fe particles are not observed in their XRD patterns, indicating that Fe NPs in $Fe_{Fe-O-Fe}$-UP/CA and Fe-SA/CA catalysts are totally removed. In addition, the elemental Fe in the format of $Fe_{Fe-O-Fe}$-UP/CA is not in the metallic Fe state, but inlaid within the carbon framework, like that in Fe-SA/CA catalysts.

The Raman spectra of carbon-based materials usually consist of two peaks, which are called the D band (at about 1331 cm^{-1}) and G band (at about 1586 cm^{-1}), respectively (Fig. 2b). The D band and G band in carbon materials represent defects and graphite carbon in the carbon, respectively.[41,42] In addition, the degree of graphitization of carbon materials can be evaluated by the intensity ratio of the D band to G band (I_D/I_G). The intensity ratios of I_D/I_G of C_{ZIF} materials, $C_{ZIF\text{-}TA}$ catalysts, Fe-SA/CA catalysts and $Fe_{Fe-O-Fe}$-UP/CA catalysts are 1.44,

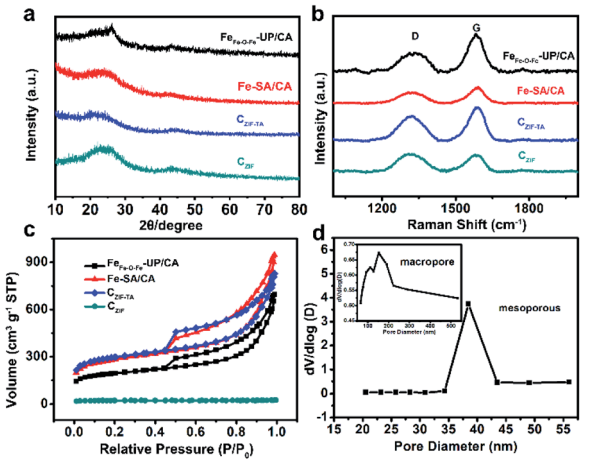

Fig. 2 (a) XRD patterns, (b) Raman spectra, (c) N_2 adsorption/desorption isotherms of $Fe_{Fe-O-Fe}$-UP/CA catalysts (black curve), Fe-SA/CA catalysts (red curve), $C_{ZIF\text{-}TA}$ catalysts (blue curve) and C_{ZIF} materials (cyan curve) and (d) pore size distributions of $Fe_{Fe-O-Fe}$-UP/CA catalysts based on the BJH method. The inset in (d) is the macropore size distribution of $Fe_{Fe-O-Fe}$-UP/CA catalysts.

1.12, 1.10 and 0.91, respectively (Fig. 2b and Table S1, ESI†). The lower the ratio of I_D/I_G, the higher the degree of graphitization of carbon materials. Thus, $Fe_{Fe-O-Fe}$-UP/CA catalysts have the highest content of graphitic carbon among them. It is found that the I_D/I_G value of C_{ZIF} materials is far bigger than that of $C_{ZIF\text{-}TA}$ catalysts, indicating that the introduction of TA can improve the degree of graphitization of carbon materials by the formation of graphene-like flaky-carbon materials. In addition, the I_D/I_G value of $C_{ZIF\text{-}TA}$ catalysts is close to that of Fe-SA/CA catalysts and bigger than that of $Fe_{Fe-O-Fe}$-UP/CA catalysts. The results indicate that the utilization of a low amount of Fe has little impact on the degree of graphitization of carbon in Fe-SA/CA catalysts. However, with increasing amount of the Fe precursor, the degree of graphitization of carbon in $Fe_{Fe-O-Fe}$-UP/CA is greatly improved, which could contribute to the enhancement in their ORR performance due to the increase in conductivity of the $Fe_{Fe-O-Fe}$-UP/CA catalysts.[43] The results are also in good agreement with their XRD results.

N_2 adsorption/desorption measurements of $Fe_{Fe-O-Fe}$-UP/CA catalysts were carried out to gain insight into their surface area and porosity property. C_{ZIF} materials, $C_{ZIF\text{-}TA}$ catalysts, and Fe-SA/CA catalysts were also investigated for comparison (Fig. 2c and d). The BET specific surface areas of C_{ZIF} materials, $C_{ZIF\text{-}TA}$ catalysts, Fe-SA/CA catalysts and $Fe_{Fe-O-Fe}$-UP/CA catalysts are calculated to be about 69.7 $m^2\ g^{-1}$, 957.3 $m^2\ g^{-1}$, 916.8 $m^2\ g^{-1}$ and 628.8 $m^2\ g^{-1}$, respectively. The result shows that the BET value of C_{ZIF} materials obtained by pyrolysis of solid ZIF particles (cyan curve) is far lower than that of $C_{ZIF\text{-}TA}$ catalysts obtained by pyrolysis of hollow ZIF particles by TA-etching (blue curve), indicating that the transformation of solid ZIF particles into hollow ZIF particles by TA-etching indeed can greatly improve their specific surface area. In addition, the BET values of $C_{ZIF\text{-}TA}$ catalysts and Fe-SA/CA catalysts are nearly equal because they have a similar morphology, which is mainly composed of hollow carbon spheres, and the presence of Fe atoms in Fe-SA/CA catalysts does not impact their specific surface areas. However, the BET value of $Fe_{Fe-O-Fe}$-UP/CA catalysts greatly decreases with increasing utilization of additional Fe(III) ions, possibly due to the decreasing ratio of hollow carbon spheres and the increasing ratio of CNTs in the CAs (Fig. S7a and b, ESI†). Moreover, $C_{ZIF\text{-}TA}$ catalysts, Fe-SA/CA catalysts and $Fe_{Fe-O-Fe}$-UP/CA catalysts have the same N_2 adsorption/desorption isotherms. The distinguishable type-IV hysteresis loop at medium and high relative pressure ($0.4 < P/P_0 < 1$) demonstrates the existence of a mesoporous structure while the sharp increase again at high relative pressure ($0.95 < P/P_0 < 1$) indicates the presence of macropores (Fig. 2c).[6,44,45] In addition, $C_{ZIF\text{-}TA}$ catalysts, Fe-SA/CA catalysts and $Fe_{Fe-O-Fe}$-UP/CA catalysts all have a mesoporous-dominant hierarchical structure (about 38 nm) accompanied by macropores from 90 to 300 nm (Fig. 2d, S17 and S18, ESI†), based on the pore size distribution curves obtained *via* the Barrett–Joyner–Halenda (BJH) method. The pore size distributions of $C_{ZIF\text{-}TA}$ catalysts, Fe-SA/CA catalysts and $Fe_{Fe-O-Fe}$-UP/CA catalysts are also well consistent with their corresponding TEM results (Fig. S7a, S12b, ESI† and 1b). Briefly, the hierarchical pore structure of $Fe_{Fe-O-Fe}$-UP/CA catalysts would favor for the diffusion of oxygen and thus benefit the improvement of their ORR performance.

To unravel the surface composition and electronic structure of their elements in $Fe_{Fe-O-Fe}$-UP/CA catalysts, X-ray photoelectron spectroscopy (XPS) analysis was carried out (Fig. 3). As shown in Fig. 3a, elemental C (86.31 wt%), N (1.8 wt%), O (11.18 wt%), and Fe (0.71 wt%) are observed in their full survey spectrum, which is in good agreement with the elemental mapping results (Fig. S15, ESI†). In contrast, the Fe 2p signal in the XPS full survey spectrum of the $Fe_{Fe-O-Fe}$-UP/CA catalysts is rather weak, possibly because Fe-UPs mainly distributed in the inner parts of the $Fe_{Fe-O-Fe}$-UP/CA catalysts after the acid-leaching treatment. There are four peaks centered at around 284.6, 285.6, 286.8, and 289.8 eV in the high-resolution C 1s spectrum of $Fe_{Fe-O-Fe}$-UP/CA catalysts (Fig. S19, ESI†), corresponding to sp^2 C (59.54%), sp^3 C (20.87%), C–O (10.75%), and C=O (8.83%) group, respectively.[29,46,47] In addition, the presence of the strongest peak of sp^2 C (Table S3, ESI†) indicates that $Fe_{Fe-O-Fe}$-UP/CA catalysts can have a high electrical conductivity.[42]

In the high-resolution N 1s spectrum of $Fe_{Fe-O-Fe}$-UP/CA catalysts (Fig. 3b), there also exist four types of N species, which are pyridinic N centered at 398.6 eV (46.75%), pyrrolic N centered at 400.45 eV (13.89%), graphitic N centered at 401.24 eV (32.84%) and oxidized N centered at 403.7 eV (6.51%), respectively.[48] In contrast, the contents of both the pyridinic N (46.75%) and graphitic N (32.84%) in $Fe_{Fe-O-Fe}$-UP/CA catalysts are higher than those (40.21% and 30.74%) in $C_{ZIF\text{-}TA}$ catalysts (Fig. S20, S21 and Table S4, ESI†), indicating that the introduction of Fe may promote their contents by the formation of CNTs. Moreover, the presence of a high content of the pyridinic N (46.75%) in $Fe_{Fe-O-Fe}$-UP/CA catalysts will improve the oxygen adsorption capacity and the onset potential of catalysts effectively because they can enhance the surface wettability and increase the electron donor of carbon materials.[8] Furthermore, the presence of a high content of the graphitic N in $Fe_{Fe-O-Fe}$-UP/CA catalysts (32.84%) induced by the formation of

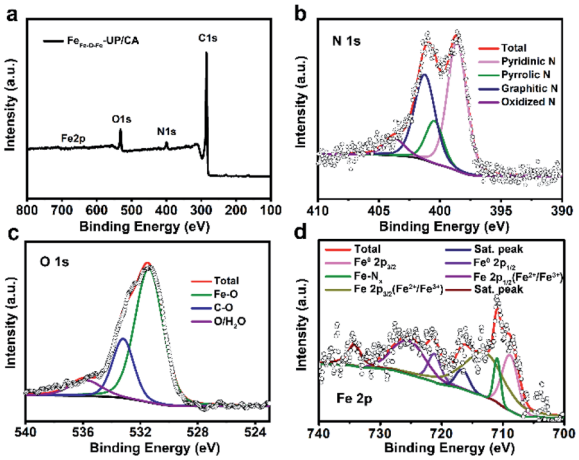

Fig. 3 (a) XPS full survey spectrum and the corresponding high-resolution spectra of (b) N 1s, (c) O 1s, and (d) Fe 2p of $Fe_{Fe-O-Fe}$-UP/CA catalysts.

a certain ratio of CNTs in CAs would benefit the improvement in their limit diffusion current density by increasing their electrical conductivity.[40] Therefore, the co-existence of pyridinic N and graphitic N in the $Fe_{Fe-O-Fe}$-UP/CA catalysts would be beneficial to the ORR performance. In the high resolution O 1s spectrum of $Fe_{Fe-O-Fe}$-UP/CA catalysts (Fig. 3c), the presence of the signal peak centered at about 531.4 eV is the evidence for the formation of the Fe–O bond in $Fe_{Fe-O-Fe}$-UP/CA catalysts after the pyrolysis of Fe–O chelation existing in the complex of TA and Fe precursors.[31] In addition, the peaks centered at about 533.2 eV and 535.8 eV are attributed to the C–O bond and adsorption of O/H_2O owing to exposure to the atmosphere, respectively. As depicted in Fig. 3d, the high-resolution Fe 2p signals of $Fe_{Fe-O-Fe}$-UP/CA catalysts can be deconvoluted into seven peaks, namely Fe^0 $2p_{3/2}$ (708.8 eV) and Fe^0 $2p_{1/2}$ (721.2 eV), Fe $2p_{3/2}$ (Fe^{2+}/Fe^{3+} ions, 713 eV) and Fe $2p_{1/2}$ (Fe^{2+}/Fe^{3+} ions, 725.4 eV), satellite peaks (716.6 and 734.2 eV), and Fe–N_x species (711 eV),[2,49] respectively. The presence of the peak (711 eV) indicates the existence of the Fe–N_x structure.[50,51] The presence of satellite peaks demonstrates that both Fe(III) and Fe(II) exist in $Fe_{Fe-O-Fe}$-UP/CA catalysts.[52] However, it is rather difficult to distinguish 2p signals of Fe^{2+} ions from those of Fe^{3+} ions. In our case, 2p signals of Fe $2p_{3/2}$ and Fe $2p_{1/2}$ are close to those of Fe^{3+} ions. It is known that Fe atoms can form bonds with uncapped sites on carbon materials, which can induce charge transfer between Fe atoms and carbon materials.[53] Accordingly, Fe atoms may also bear a positive charge by electronic interaction between Fe atoms and the local surrounding atoms (such as C, O, and N atoms) in our $Fe_{Fe-O-Fe}$-UP/CA catalysts, which will be verified by the results of X-ray absorption near-edge structure (XANES) spectroscopy and extended X-ray absorption fine structure (EXAFS) spectroscopy.

XANES and EXAFS were utilized to further understand the local atomic coordination and electronic structure around Fe atoms in $Fe_{Fe-O-Fe}$-UP/CA catalysts. Fe foil, iron phthalocyanine (FePc), and Fe_2O_3 were also measured for comparison (Fig. 4). As shown in Fig. 4a, the absorption edge of $Fe_{Fe-O-Fe}$-UP/CA catalysts is located between that of FePc and Fe_2O_3, indicating that the oxidation state of Fe atoms is between +2 and +3 in $Fe_{Fe-O-Fe}$-UP/CA catalysts.[54,55] In addition, one rather weak pre-edge peak at about 7113 eV can be seen in the XANES spectra of $Fe_{Fe-O-Fe}$-UP/CA catalysts, which is rather similar to that of Fe_2O_3 (without energy calibration, Fig. 4a). The result indicates that the coordination configuration of the atoms surrounding Fe atoms in the $Fe_{Fe-O-Fe}$-UP/CA catalysts forms a 6-fold coordination structure.[56–58] Moreover, the EXAFS is further deduced from the Fe K-edge spectra and fitted using the Demeter software package to obtain more information on the Fe-ligand structure in the $Fe_{Fe-O-Fe}$-UP/CA catalysts. As shown in Fig. 4b and S22a (ESI†), the Fourier transform (FT) of the k^3-weighted K-edge EXAFS spectrum of the $Fe_{Fe-O-Fe}$-UP/CA catalysts is apparently different from that of Fe foil, demonstrated by the absence of the strong Fe–Fe scattering peaks at 2.2 Å,[59] and it indicates the absence of metallic Fe particles in the as-prepared $Fe_{Fe-O-Fe}$-UP/CA catalysts, which is in good agreement with the XRD and XPS results. In contrast, the well-matched major peak located at 1.5 Å exists in the FT-EXAFS spectra of both the $Fe_{Fe-O-Fe}$-UP/CA catalysts and FePc (Fig. S22b, ESI†), indicating that Fe–N_4 moieties should be present in our $Fe_{Fe-O-Fe}$-UP/CA catalysts.[33,60] Accordingly, it can be concluded that the Fe atoms interacted with neighboring four N atoms in $Fe_{Fe-O-Fe}$-UP/CA catalysts. Furthermore, the scattering peaks located at around 2.6 Å and 3.1 Å, which are ascribed to the second shell of Fe–Fe bond, were detected in the FT-EXAFS spectra of $Fe_{Fe-O-Fe}$-UP/CA catalysts. These peaks of Fe-UPs in $Fe_{Fe-O-Fe}$-UP/CA catalysts are similar to those of Fe_2O_3 (Fig. S22c, ESI†). These results indicate that the Fe–O bond should exist in Fe-UPs in the $Fe_{Fe-O-Fe}$-UP/CA catalysts, which is in good agreement with XPS results. However, the difference in their intensity also indicates the difference in the coordination configuration of Fe atoms between Fe_2O_3 and Fe-UPs in $Fe_{Fe-O-Fe}$-UP/CA catalysts. In view of the presence of the Fe–N_4 and Fe–O bond, it is highly possible that Fe-UPs are composed of the Fe–N_4–O_x–Fe–N_4 moiety. However, the number of O atoms between two Fe atoms still needs to be determined.

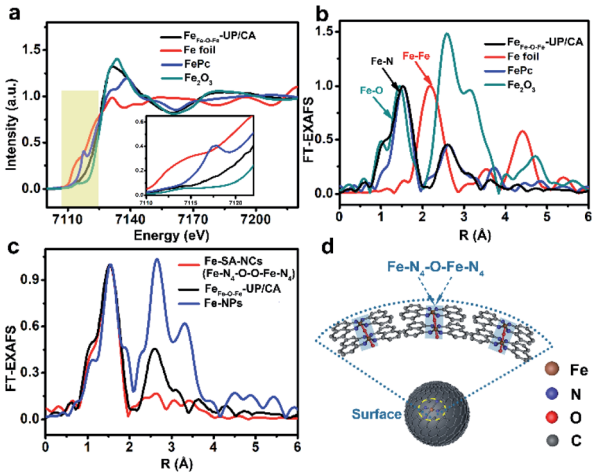

Fig. 4 (a) Fe K-edge XANES spectra and the enlarged image of the pre-edge (the inset in a), (b) FT-EXAFS spectra of $Fe_{Fe-O-Fe}$-UP/CA catalysts, Fe foil, FePc and Fe_2O_3, (c) FT-EXAFS spectra of Fe–N_4–O–O–Fe–N_4 in Fe-SA-NCs catalysts, $Fe_{Fe-O-Fe}$-UP/CA catalysts and Fe-NP catalysts, (d) schematic model of the local atomic configuration around Fe atoms in $Fe_{Fe-O-Fe}$-UP/CA catalysts.

To further determine the coordination configuration of Fe atoms of Fe-UPs in $Fe_{Fe-O-Fe}$-UP/CA catalysts, FT-EXAFS curves of $Fe_{Fe-O-Fe}$-UP/CA catalysts, Fe-SA-NCs catalysts with NCs sizes of about 0.5–1.5 nm and Fe-NP-based catalysts with NPs sizes of about 3.8 nm are combined together for better comparison (Fig. 4c, S22d and e, ESI†). It is obvious that the size of Fe-UPs in the $Fe_{Fe-O-Fe}$-UP/CA catalysts is larger than that of NCs in the Fe-SA-NCs catalysts but smaller than that of Fe-NP in the traditional Fe-NP-based catalysts. Interestingly, the intensity of the Fe–Fe peaks (located at 2.6 Å and 3.1 Å) of Fe-UPs in the $Fe_{Fe-O-Fe}$-UP/CA catalysts is stronger than that of NCs in the Fe-SA-NC catalysts but weaker than that of Fe-NPs in the traditional Fe-NP catalysts. In addition, the FT-EXAFS curve of $Fe_{Fe-O-Fe}$-UP/CA catalysts is rather similar to that of the Fe–N_4–O–Fe–N_4 moiety as active sites reported recently (Fig. S22f, ESI†).[31] Moreover, in our previous work, the active sites in NCs with sizes of about

0.5–1.5 nm in the Fe-SA-NC catalysts are the Fe–N_4–O–O–Fe–N_4 moieties while Fe–Fe bonds are present in the traditional Fe-NP-based catalyst. Furthermore, it has been proposed that the number of oxygen atom decreases with increasing size of Fe-atom-based particles (Fig. S23, ESI†).[29] Bearing these in mind, it is highly possible that the active sites in Fe-UPs of $Fe_{Fe-O-Fe}$-UP/CA catalysts are the Fe–N_4–O–Fe–N_4 moieties. Given the similarity and difference among $Fe_{Fe-O-Fe}$-UP/CA catalysts, the Fe–N_4–O–Fe–N_4-based catalyst, Fe-SA-NCs catalysts and Fe-NP catalysts, the local atomic configuration around Fe atoms in $Fe_{Fe-O-Fe}$-UP/CA catalysts is proposed as follows: (a) the coordination number of each Fe atom is six; (b) each Fe atom in Fe-UPs of $Fe_{Fe-O-Fe}$-UP/CA catalysts is coordinated with four N atoms and one O atom; (c) each Fe-UP is composed of tens of Fe–N_4–O–Fe–N_4 moieties; and (d) each Fe–N_4 moiety is separated by one O atom (Fig. 4d).[31,61] Fe-UPs in $Fe_{Fe-O-Fe}$-UP/CA catalysts are composed of the Fe–N_4–O–Fe–N_4 moiety, instead of pure Fe atoms. Similarly, the formation of the Fe–O–Fe bond in the Fe-UPs results from the complexes of Fe^{3+} ions and hydroxyl groups (OH^-) of TA during the pyrolysis.

Electrocatalytic performance of $Fe_{Fe-O-Fe}$-UP/CA catalysts towards the ORR

The catalytic performance of $Fe_{Fe-O-Fe}$-UP/CA catalysts was first assessed by cyclic voltammetry (CV) measurements in O_2-saturated 0.1 M KOH electrolyte and the commercial Pt/C catalyst (Johnson Matthey, 20 wt%) was also investigated as a reference electrocatalyst (Fig. S24, ESI†). Both exhibit well-defined oxygen reduction peaks in the O_2-saturated KOH electrolyte and only electrochemical double-layer capacitance was detected with the N_2-saturated electrolyte. In addition, the potential of the oxygen reduction peak of the $Fe_{Fe-O-Fe}$-UP/CA catalysts is 0.90 V *versus* the reversible hydrogen electrode (*vs.* RHE), which is much higher than that (0.86 V *vs.* RHE) of the commercial Pt/C catalyst, indicating the superior ORR catalytic activity of $Fe_{Fe-O-Fe}$-UP/CA catalysts in alkaline media.[62] The ORR performances of $Fe_{Fe-O-Fe}$-UP/CA catalysts, Fe-SA/CA catalysts, the commercial Pt/C catalyst and C_{ZIF-TA} catalysts were further investigated by LSV measurements with a rotating disk electrode (RDE) at a scan rate of 5 mV s^{-1} in O_2-saturated 0.1 M KOH at 1600 rpm. As shown in Fig. 5a, C_{ZIF-TA} catalysts display a poor ORR performance (cyan curve) with a half-wave potential ($E_{1/2}$) of 0.82 V and an onset potential (E_{onset}) of 0.94 V, which is worse than those of the commercial Pt/C catalyst (blue curve). In contrast, Fe-SA/CA catalysts show an improved ORR performance with an $E_{1/2}$ of 0.90 V and E_{onset} of 1.03 V (red curve), which is better than those of the commercial Pt/C catalyst (blue curve). As mentioned above, C_{ZIF-TA} catalysts and Fe-SA/CA catalysts have a similar morphology and BET surface area values. Thus, the presence of favorable active sites of Fe–SAs in Fe-SA/CA catalysts should be the key to improve the ORR activity.

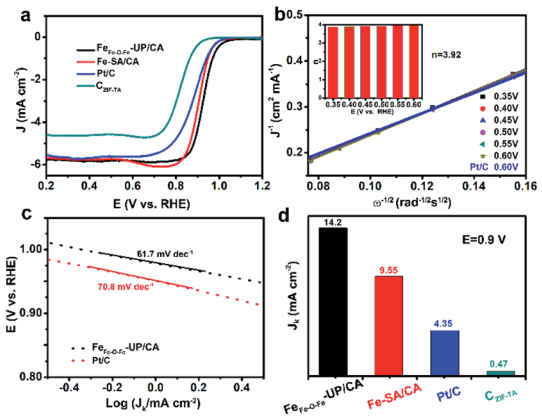

Fig. 5 (a) LSV curves of $Fe_{Fe-O-Fe}$-UP/CA catalysts (black curve), Fe-SA/CA catalysts (red curve), the commercial Pt/C catalyst (blue curve) and C_{ZIF-TA} catalysts (cyan curve), measured in O_2-saturated 0.1 M KOH at a rotation speed of 1600 rpm and a potential scan rate of 10 mv s^{-1}; (b) K–L plots of $Fe_{Fe-O-Fe}$-UP/CA catalysts at different potentials; (c) Tafel plots of $Fe_{Fe-O-Fe}$-UP/CA catalysts (black curve) and the commercial Pt/C catalyst (red curve) obtained from the RDE measurements; and (d) comparison of kinetic current density (J_k) at 0.9 V of $Fe_{Fe-O-Fe}$-UP/CA catalysts (black), Fe-SA/CA catalysts (red), the commercial Pt/C catalyst (blue) and C_{ZIF-TA} catalysts (cyan).

Compared with Fe-SA/CA catalysts and Fe-NP/CA catalysts, $Fe_{Fe-O-Fe}$-UP/CA catalysts have a smaller BET surface area value and a lower ratio of CNTs in CAs, respectively. However, the $E_{1/2}$ value (0.93 V) and E_{onset} value (1.08 V) of $Fe_{Fe-O-Fe}$-UP/CA catalysts are more positive than those of Fe-SA/CA catalysts ($E_{1/2}$ of 0.90 V and E_{onset} of 1.03 V) and Fe-NP/CA catalysts ($E_{1/2}$ of 0.90 V and E_{onset} of 1.02 V) (Fig. S25, ESI†). Thus, the results indicate that the enhancement in ORR activity of $Fe_{Fe-O-Fe}$-UP/CA catalysts is mainly attributed to the formation of a new type of active site (Fe–N_4–O–Fe–N_4 moiety), which will be discussed later, instead of their improved degree of graphitization in the presence of abundant of CNTs.[63] In addition, the ORR activity of $Fe_{Fe-O-Fe}$-UP/CA catalysts ($E_{1/2}$ = 0.93 V and E_{onset} = 1.08 V) is higher than that ($E_{1/2}$ = 0.89 V and E_{onset} = 1.00 V) of the commercial Pt/C catalyst and the most of Fe-based catalysts reported in the literature thus far (Table S6, ESI†), possibly because of the presence of new type of active sites, the large surface area and the higher degree of graphitization. In our case, the size of Fe-UPs in the as-prepared $Fe_{Fe-O-Fe}$-UP/CA catalysts is in the range of 2–3 nm. Thus, the adsorption strength of O_2 to Fe atoms in the Fe–N_4–O–Fe–N_4 moiety of Fe-UPs would be enhanced[31] due to their increasing size, compared with SACs. Moreover, the bridging O atom in the Fe–N_4–O–Fe–N_4 moiety would act as an electronic structure modifier to weaken the bonding strength between Fe and ORR intermediates. Accordingly, the as-prepared $Fe_{Fe-O-Fe}$-UP/CA catalysts can achieve the balance between the adsorption of reactants and the desorption of intermediates and products due to their increasing size and the presence of the multi-metal-atom structure. Thus, the as-prepared $Fe_{Fe-O-Fe}$-UP/CA catalysts can show improved ORR activity by improving the adsorption strength to O_2 (*O_2 binding energy) and lowering the formation energy of the *O intermediate.

The ORR kinetics of $Fe_{Fe-O-Fe}$-UP/CA catalysts was investigated using the RDE technique at different rotation speeds (Fig. S26, ESI†). In addition, the electron transfer number of $Fe_{Fe-O-Fe}$-UP/CA catalysts towards the ORR was calculated based

on the Koutecky–Levich (K–L) equation plots. As shown in Fig. 5b, the electron transfer number of $Fe_{Fe-O-Fe}$-UP/CA was calculated to be 3.92, which is rather close to that of the commercial Pt/C catalyst (Fig. S27, ESI†), indicating the desirable four-electron transfer process for the ORR catalyzed by $Fe_{Fe-O-Fe}$-UP/CA mainly. In contrast, the electron transfer numbers of Fe-SA/CA catalysts and C_{ZIF-TA} catalysts are calculated to be 3.6 and 3.0 (Fig. S28 and S29, ESI†), respectively. The results suggest that active sites (Fe–N_4–O–Fe–N_4 moiety) in $Fe_{Fe-O-Fe}$-UP/CA catalysts indeed play a key role in electrocatalytic selectivity, compared with those in Fe-SA/CA catalysts (Fe–SAs) and C_{ZIF-TA} catalysts (carbon defects).

The Tafel plots of $Fe_{Fe-O-Fe}$-UP/CA catalysts and the commercial Pt/C catalyst are shown in Fig. 5c. The Tafel slope of $Fe_{Fe-O-Fe}$-UP/CA catalysts (61.7 mV dec^{-1}) under alkaline conditions is lower than that for the commercial Pt/C catalyst (70.8 mV dec^{-1}). Such a kinetic process for ORR activity catalyzed by $Fe_{Fe-O-Fe}$-UP/CA catalysts is more effective than that by the commercial Pt/C catalyst. This is because the lower Tafel slope indicates higher ORR activity.[64] Moreover, the kinetic current density of $Fe_{Fe-O-Fe}$-UP/CA catalysts was calculated from the intercept of the linearly fitted K-L plots to be 14.2 mA cm^{-2} at 0.9 V, which was much higher than that of Fe-SA/CA catalysts (9.55 mA cm^{-2}), the commercial Pt/C catalyst (4.35 mA cm^{-2}), and C_{ZIF-TA} catalysts (0.47 mA cm^{-2}) (Fig. 5d). These results further indicate the synergistic advantages of a hierarchical micro-macro structure and desired newly active components in $Fe_{Fe-O-Fe}$-UP/CA catalysts for the ORR.

In addition to the ORR activities, the durability of $Fe_{Fe-O-Fe}$-UP/CA catalysts toward the ORR in an alkaline electrolyte was further evaluated by the chronoamperometric method, cycling test and methanol-crossover effect test, in comparison with the commercial Pt/C catalyst (Fig. 6). After the continuous chronoamperometric measurement for 12 000 s in O_2-saturated 0.1 M KOH electrolyte (Fig. 6a), $Fe_{Fe-O-Fe}$-UP/CA catalysts preserved almost a constant current plateau with an initial drop of only 2.7% at 0.90 V, whereas the commercial Pt/C catalyst suffers from a gradual current loss of about 32% with respect to its initial current density. The less current decay at $Fe_{Fe-O-Fe}$-UP/CA catalysts confirms the superior electrochemical stability. Moreover, the durability of $Fe_{Fe-O-Fe}$-UP/CA catalysts was further assessed by using the accelerated durability test (ADT) between 0.2 and 1.0 V at a sweep rate of 100 mV s^{-1} in O_2-saturated 0.1 M KOH for 5000 cycles. As shown in Fig. 6b, the $E_{1/2}$ value of $Fe_{Fe-O-Fe}$-UP/CA catalysts is almost unchanged while that of the commercial Pt/C catalyst displays a negative shift of 12 mV after ADT of 5000 cycles (Fig. S30, ESI†), further demonstrating the excellent stability of $Fe_{Fe-O-Fe}$-UP/CA catalysts. Furthermore, the methanol tolerances of $Fe_{Fe-O-Fe}$-UP/CA catalysts and the commercial Pt/C catalyst in an alkaline electrolyte were investigated by using their chronoamperometric responses. As shown in Fig. 6c, no significant current change in the chronoamperometric curve of $Fe_{Fe-O-Fe}$-UP/CA is observed, whereas an instantaneous jump decrease in the chronoamperometric curve of the commercial Pt/C catalyst is observed after the addition of 3 M methanol into the electrolyte, suggesting the excellent tolerance of $Fe_{Fe-O-Fe}$-UP/CA catalysts against methanol crossover effects. Briefly, all these results indicate that $Fe_{Fe-O-Fe}$-UP/CA catalysts indeed have much better ORR performance, stability, and selectivity than the commercial Pt/C catalyst in alkaline media.

To demonstrate the potential in real energy devices, a Zn-air battery (ZAB) was further fabricated by using Zn foil as the anode, $Fe_{Fe-O-Fe}$-UP/CA catalysts as the cathode, and 6 M KOH with 0.2 M zinc acetate as the electrolyte (Fig. 7a), since they have a superior ORR performance in alkaline media. Fe-SA/CA catalysts and the commercial Pt/C catalyst as the cathode electrocatalysts were also investigated for comparison. The stable open-circuit voltage (OCV) of the ZAB assembled with $Fe_{Fe-O-Fe}$-UP/CA catalysts is 1.49 V (Fig. 7b), which is higher than that of the commercial Pt/C catalyst (1.43 V), Fe-SA/CA catalysts (1.46 V) and Fe-NP/CA catalysts (1.48 V) (Fig. S31, ESI†), indicating their good practical performance. Their discharge polarization curves and the corresponding power density curves are shown in Fig. 7c. It can be clearly seen that the ZAB assembled with Fe_{Fe-}

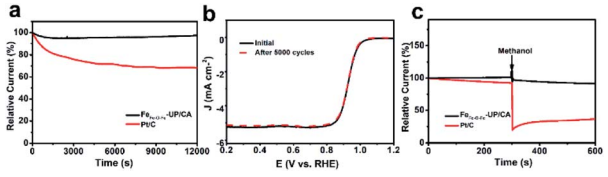

Fig. 6 (a) Chronoamperometric responses to durability evaluation of $Fe_{Fe-O-Fe}$-UP/CA catalysts and the commercial Pt/C catalyst at 0.9 V *vs.* RHE, measured in O_2-saturated 0.1 M KOH, (b) ORR LSVs of $Fe_{Fe-O-Fe}$-UP/CA catalysts before and after 5000 cycles in O_2-saturated 0.1 M KOH, and (c) methanol-crossover effect test results of $Fe_{Fe-O-Fe}$-UP/CA catalysts and the commercial Pt/C catalyst to the addition of methanol in O_2-saturated 0.1 M KOH.

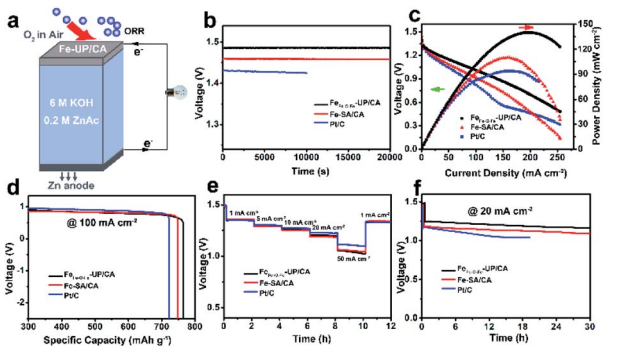

Fig. 7 (a) Schematic illustration of the model of a primary Zn-air battery, (b) open-circuit plots of the primary Zn-air batteries with different catalysts, (c) discharge polarization curves and the corresponding power density curves of the primary Zn-air batteries with different catalysts, (d) specific capacities at a current density of 100 mA cm^{-2} of $Fe_{Fe-O-Fe}$-UP/CA catalysts, Fe-SA/CA catalysts and the commercial Pt/C catalyst based primary Zn-air battery, (e) galvanostatic discharge curves of primary Zn-air batteries with different catalysts at different current densities, and (f) long-time discharge curves of the primary Zn-air batteries with different catalysts at the current density of 20 mA cm^{-2}. For better comparison, $Fe_{Fe-O-Fe}$-UP/CA catalysts, Fe-SA/CA catalysts, and the commercial Pt/C catalyst are shown as black curves, red curve, and blue curves, respectively.

$_{O-Fe}$-UP/CA catalysts presents the maximum power density of 140.1 mW cm^{-2} at a current density of 197.3 mA cm^{-2}, which is much higher than that with the commercial Pt/C catalyst (93.7 mW cm^{-2} at 161.7 mA cm^{-2}) and far higher than that with Fe-SA/CA catalysts (109.8 mW cm^{-2} at 157.9 mA cm^{-2}) and that with Fe-NP/CA catalysts (101.0 mW cm^{-2} at 128.6 mA cm^{-2}) (Fig. S32, ESI†). It is found that the power density of the ZAB assembled with $Fe_{Fe-O-Fe}$-UP/CA catalysts is also comparable to those of the ZABs assembled with Fe-SA catalysts reported in the literature (Table S7, ESI†). As shown in Fig. 7d, the specific capacity of the ZAB assembled with $Fe_{Fe-O-Fe}$-UP/CA catalysts can be up to 781.7 mA h g^{-1} at a current density of 100 mA cm^{-2}, which is significantly superior to that with Fe-SA/CA (752 mA h g^{-1}) and Fe-NP/CA catalysts (673 mA h g^{-1}) (Fig. S33, ESI†) and higher than that with the commercial Pt/C catalyst (731 mA h g $^{-1}$ at 100 mA cm^{-2}). Galvanostatic discharge curves (Fig. 7e) clearly demonstrate the good stability of the ZAB consisting of $Fe_{Fe-O-Fe}$-UP/CA catalysts when changing the current density from 1 mA cm^{-2} to a much larger current density of 50 mA cm^{-2}. More significantly, the initial and final voltages at 1 mA cm^{-2} of the ZAB consisting of $Fe_{Fe-O-Fe}$-UP/CA catalysts are rather close (1.35 V and 1.33 V, respectively), indicating their robust long-term discharging capability. The results also exhibit the good high-rate performance of the Zn-air battery with $Fe_{Fe-O-Fe}$-UP/CA catalysts, which is in good agreement with the larger power density. In addition, on the basis of the long-time galvanostatic discharge curves at a constant current density of 20 mA cm^{-2} (Fig. 7f), it can be seen that the voltage of the primary ZAB consisting of $Fe_{Fe-O-Fe}$-UP/CA catalysts is higher than that of the ZAB consisting of Fe-SA/CA catalysts or the commercial Pt/C catalyst. The result also exhibits that the primary ZAB consisting of $Fe_{Fe-O-Fe}$-UP/CA catalysts has a good catalytic stability during cell operation even at relatively large current. The slight decrease in the voltage of the ZAB consisting of $Fe_{Fe-O-Fe}$-UP/CA catalysts may be caused by the absorption of CO_2 from the atmosphere into the electrolyte.[65] Briefly, all of these results demonstrate that $Fe_{Fe-O-Fe}$-UP/CA catalysts not only can exhibit a high-performance towards the ORR, but also can be applied to the ZABs as a potential air cathode electrocatalyst.

Conclusions

In summary, we successfully prepared $Fe_{Fe-O-Fe}$-UP/CA catalysts with 2–3 nm Fe-UPs consisting of new types of active sites (Fe–N_4–O–Fe–N_4 moiety). Moreover, Fe-UPs consisting of the Fe–N_4–O–Fe–N_4 moiety ($Fe_{Fe-O-Fe}$-UPs) in Fe-UP/CA catalysts are realized by controlling the Fe-to-TA molar ratio at 2.2 under other fixed reaction conditions. Each Fe–N_4 moiety within these Fe-UPs is separated by one O atom and each Fe atom in the Fe–N_4–O–Fe–N_4 moiety is coordinated with four N atoms and one O atom. Due to their increasing size and the presence of the multi-metal-atom structure, the as-prepared $Fe_{Fe-O-Fe}$-UP/CA catalysts can achieve the balance between the adsorption of reactants and the desorption of intermediates and products. Accordingly, the resulting $Fe_{Fe-O-Fe}$-UP/CA catalysts towards the ORR in alkaline media exhibit a higher half-wave potential (0.93 V *vs.* 0.89 V of Pt/C), a higher onset potential (1.08 V *vs.* 1.00 V of Pt/C), a higher kinetic current density (14.2 mA cm^{-2} at 0.9 V) and better long-term stability. In addition, the $Fe_{Fe-O-Fe}$-UP/CA catalysts show much better ORR performance than those with Fe–SAs and comparable to those with Fe-SA-NCs. Moreover, the ZABs assembled with $Fe_{Fe-O-Fe}$-UP/CA catalysts as an air cathode also exhibit a high discharge voltage (1.49 V), a high power density (140.1 mW cm^{-2} at 197.3 mA cm^{-2}), a high specific capacity (781.7 mA h g^{-1}) and good stability, which are better than those of the state-of-the-art the commercial Pt/C catalyst. Furthermore, our synthetic strategy presented here can be extended to prepare carbon aerogels decorated with other metal ultra-small particles consisting of new active sites of the MN_4-O-MN_4 moiety as electrocatalysts for the ORR, OER and HER, given the chelation ability of TA with diverse metal ions.

Conflicts of interest

There are no conflicts to declare.

Acknowledgements

This work is financially supported by the Natural Science Foundation of China (21773142 and 22072076), the Taishan Scholarship in Shandong Province (No. tsqn20161001) and Fundamental Research Fund of Shandong University.

References

1 X. F. Lu, S. L. Zhang, E. Shangguan, P. Zhang, S. Gao and X. W. Lou, *Adv. Sci.*, 2020, **7**, 2001178.
2 Y. Lei, F. Yang, H. Xie, Y. Lei, X. Liu, Y. Si and H. Wang, *J. Mater. Chem. A*, 2020, **8**, 20629–20636.
3 J. Huo, L. Lu, Z. Shen, Y. Liu, J. Guo, Q. Liu, Y. Wang, H. Liu, M. Wu and G. Wang, *J. Mater. Chem. A*, 2020, **8**, 16271–16282.
4 Z. Chen, X. Gao, X. Wei, X. Wang, Y. Li, T. Wu, J. Guo, Q. Gu, W. D. Wu and X. D. Chen, *Carbon*, 2017, **121**, 143–153.
5 Y. Deng, B. Chi, X. Tian, Z. Cui, E. Liu, Q. Jia, W. Fan, G. Wang, D. Dang and M. Li, *J. Mater. Chem. A*, 2019, **7**, 5020–5030.
6 X. Peng, L. Zhang, Z. Chen, L. Zhong, D. Zhao, X. Chi, X. Zhao, L. Li, X. Lu and K. Leng, *Adv. Mater.*, 2019, **31**, 1900341.
7 X. Zhang, X. Han, Z. Jiang, J. Xu, L. Chen, Y. Xue, A. Nie, Z. Xie, Q. Kuang and L. Zheng, *Nano Energy*, 2020, **71**, 104547.
8 I. S. Amiinu, X. Liu, Z. Pu, W. Li, Q. Li, J. Zhang, H. Tang, H. Zhang and S. Mu, *Adv. Funct. Mater.*, 2018, **28**, 1704638.
9 X. Zhu, D. Zhang, C. J. Chen, Q. Zhang, R. S. Liu, Z. Xia, L. Dai, R. Amal and X. Lu, *Nano Energy*, 2020, **71**, 104597.
10 D. Chen, J. Zhu, X. Mu, R. Cheng, W. Li, S. Liu, Z. Pu, C. Lin and S. Mu, *Appl. Catal., B*, 2020, **268**, 118729.
11 G. Ye, Q. He, S. Liu, K. Zhao, Y. Su, W. Zhu, R. Huang and Z. He, *J. Mater. Chem. A*, 2019, **7**, 16508–16515.
12 S. Han, X. Hu, J. Wang, X. Fang and Y. Zhu, *Adv. Energy Mater.*, 2018, **8**, 1800955.

13 M. Xiao, J. Zhu, L. Ma, Z. Jin, J. Ge, X. Deng, Y. Hou, Q. He, J. Li and Q. Jia, *ACS Catal.*, 2018, **8**, 2824–2832.
14 X. Sun, P. Wei, S. Gu, J. Zhang, Z. Jiang, J. Wan, Z. Chen, L. Huang, Y. Xu and C. Fang, *Small*, 2020, **16**, 1906057.
15 Y. Chen, R. Gokhale, A. Serov, K. Artyushkova and P. Atanassov, *Nano Energy*, 2017, **38**, 201–209.
16 Q. Cheng, S. Han, K. Mao, C. Chen, L. Yang, Z. Zou, M. Gu, Z. Hu and H. Yang, *Nano Energy*, 2018, **52**, 485–493.
17 X. F. Lu, Y. Chen, S. Wang, S. Gao and X. W. Lou, *Adv. Mater.*, 2019, **31**, 1902339.
18 X. F. Lu, B. Y. Xia, S. Q. Zang and X. W. Lou, *Angew. Chem., Int. Ed.*, 2020, **59**, 4634–4650.
19 H. T. Chung, D. A. Cullen, D. Higgins, B. T. Sneed, E. F. Holby, K. L. More and P. Zelenay, *Science*, 2017, **357**, 479.
20 M. Qiao, Y. Wang, Q. Wang, G. Hu, X. Mamat, S. Zhang and S. Wang, *Angew. Chem., Int. Ed.*, 2020, **59**, 2688–2694.
21 H. Zhang, S. Hwang, M. Wang, Z. Feng, S. Karakalos, L. Luo, Z. Qiao, X. Xie, C. Wang, D. Su, Y. Shao and G. Wu, *J. Am. Chem. Soc.*, 2017, **139**, 14143–14149.
22 J. H. Zagal and M. T. M. Koper, *Angew. Chem., Int. Ed.*, 2016, **55**, 14510–14521.
23 Y. He, S. Liu, C. Priest, Q. Shi and G. Wu, *Chem. Soc. Rev.*, 2020, **49**, 3484–3524.
24 D. Y. Kuo, H. Paik, J. Kloppenburg, B. Faeth, K. M. Shen, D. G. Schlom, G. Hautier and J. Suntivich, *J. Am. Chem. Soc.*, 2018, **140**, 17597–17605.
25 K. J. J. Mayrhofer and M. Arenz, *Nat. Chem.*, 2009, **1**, 518–519.
26 J. Gao, H. B. Yang, X. Huang, S. F. Hung, W. Cai, C. Jia, S. Miao, H. M. Chen, X. Yang, Y. Huang, T. Zhang and B. Liu, *Chem*, 2020, **6**, 658–674.
27 D. Y. Chung, J. M. Yoo and Y. E. Sung, *Adv. Mater.*, 2018, **30**, 1704123.
28 X. Li, L. Liu, X. Ren, J. Gao, Y. Huang and B. Liu, *Sci. Adv.*, 2020, **6**, eabb6833.
29 H. Li, K. Du, C. Xiang, P. An, X. Shu, Y. Dang, C. Wu, J. Wang, W. Du, J. Zhang, S. Li, H. Tian, S. Wang and H. Xia, *J. Mater. Chem. A*, 2020, **8**, 17136–17149.
30 M. Xiao, Y. Chen, J. Zhu, H. Zhang, X. Zhao, L. Gao, X. Wang, J. Zhao, J. Ge, Z. Jiang, S. Chen, C. Liu and W. Xing, *J. Am. Chem. Soc.*, 2019, **141**, 17763–17770.
31 L. Gong, H. Zhang, Y. Wang, E. Luo, K. Li, L. Gao, Y. Wang, Z. Wu, Z. Jin, J. Ge, Z. Jiang, C. Liu and W. Xing, *Angew. Chem., Int. Ed.*, 2020, **59**, 13923–13928.
32 S. C. Li, B. C. Hu, Y. W. Ding, H. W. Liang, C. Li, Z. Y. Yu, Z. Y. Wu, W. S. Chen and S. H. Yu, *Angew. Chem., Int. Ed.*, 2018, **57**, 7085–7090.
33 Y. Chen, S. Hu, F. Nichols, F. Bridges, S. Kan, T. He, Y. Zhang and S. Chen, *J. Mater. Chem. A*, 2020, **8**, 11649–11655.
34 Z. Y. Wu, H. W. Liang, B. C. Hu and S. H. Yu, *Angew. Chem., Int. Ed.*, 2018, **57**, 15646–15662.
35 Q. Lai, Y. Zhao, Y. Liang, J. He and J. Chen, *Adv. Funct. Mater.*, 2016, **26**, 8334–8344.
36 T. Liu, P. Zhao, X. Hua, W. Luo, S. Chen and G. Cheng, *J. Mater. Chem. A*, 2016, **4**, 11357–11364.
37 Z. Li, X. Liang, Q. Gao, H. Zhang, H. Xiao, P. Xu, T. Zhang and Z. Liu, *Carbon*, 2019, **154**, 466–477.
38 S. Hu, W. Ni, D. Yang, C. Ma, J. Zhang, J. Duan, Y. Gao and S. Zhang, *Carbon*, 2020, **162**, 245–255.
39 M. B. Gawande, P. Fornasiero and R. Zbořil, *ACS Catal.*, 2020, **10**, 2231–2259.
40 X. Chen, N. Wang, K. Shen, Y. Xie, Y. Tan and Y. Li, *ACS Appl. Mater. Interfaces*, 2019, **11**, 25976–25985.
41 L. Peng, C. T. Hung, S. Wang, X. Zhang, X. Zhu, Z. Zhao, C. Wang, Y. Tang, W. Li and D. Zhao, *J. Am. Chem. Soc.*, 2019, **141**, 7073–7080.
42 M. Hong, J. Nie, X. Zhang, P. Zhang, Q. Meng, J. Huang, Z. Xu, C. Du and J. Chen, *J. Mater. Chem. A*, 2019, **7**, 25557–25566.
43 Z. K. Yang, C. Z. Yuan and A. W. Xu, *ACS Energy Lett.*, 2018, **3**, 2383–2389.
44 S. Gao, B. Fan, R. Feng, C. Ye, X. Wei, J. Liu and X. Bu, *Nano Energy*, 2017, **40**, 462–470.
45 X. Chen, N. Wang, K. Shen, Y. Xie, Y. Tan and Y. Li, *ACS Appl. Mater. Interfaces*, 2019, **11**, 25976–25985.
46 G. Chen, P. Liu, Z. Liao, F. Sun, Y. He, H. Zhong, T. Zhang, E. Zschech, M. Chen, G. Wu, J. Zhang and X. Feng, *Adv. Mater.*, 2020, **32**, 1907399.
47 Z. Yang, C. Zhao, Y. Qu, H. Zhou, F. Zhou, J. Wang, Y. Wu and Y. Li, *Adv. Mater.*, 2019, **31**, 1808043.
48 J. Yang, J. Hu, M. Weng, R. Tan, L. Tian, J. Yang, J. Amine, J. Zheng, H. Chen and F. Pan, *ACS Appl. Mater. Interfaces*, 2017, **9**, 4587–4596.
49 H. Jin, H. Zhou, W. Li, Z. Wang, J. Yang, Y. Xiong, D. He, L. Chen and S. Mu, *J. Mater. Chem. A*, 2018, **6**, 20093–20099.
50 G. Zhang, L. Li, M. Chen and F. Yang, *J. Mater. Chem. A*, 2020, **8**, 9256–9267.
51 A. Al-Shahat Eissa, N. H. Kim and J. H. Lee, *J. Mater. Chem. A*, 2020, **8**, 23436–23454.
52 G. Li, L. Pei, Y. Wu, B. Zhu, Q. Hu, H. Yang, Q. Zhang, J. Liu and C. He, *J. Mater. Chem. A*, 2019, **7**, 11223–11233.
53 X. F. Yang, A. Wang, B. Qiao, J. Li, J. Liu and T. Zhang, *Acc. Chem. Res.*, 2013, **46**, 1740–1748.
54 Y. Chen, S. Ji, Y. Wang, J. Dong, W. Chen, Z. Li, R. Shen, L. Zheng, Z. Zhuang, D. Wang and Y. Li, *Angew. Chem., Int. Ed.*, 2017, **56**, 6937–6941.
55 J. Chen, H. Li, C. Fan, Q. Meng, Y. Tang, X. Qiu, G. Fu and T. Ma, *Adv. Mater.*, 2020, **32**, 2003134.
56 H. Fei, J. Dong, Y. Feng, C. Allen, C. Wan, B. Volosskiy, M. Li, Z. Zhao, Y. Wang, H. Sun, P. An, W. Chen, G. Zhiying, C. Lee, D. Chen, I. Shakir, M. Liu, T. Hu, Y. Li and Y. Huang, *Nat. Catal.*, 2018, **1**, 63–72.
57 U. I. Kramm, I. Herrmann-Geppert, J. Behrends, K. Lips, S. Fiechter and P. Bogdanoff, *J. Am. Chem. Soc.*, 2016, **138**, 635–640.
58 Y. J. Sa, D. J. Seo, J. Woo, J. T. Lim, J. Y. Cheon, S. Y. Yang, J. M. Lee, D. Kang, T. J. Shin, H. S. Shin, H. Y. Jeong, C. S. Kim, M. G. Kim, T. Y. Kim and S. H. Joo, *J. Am. Chem. Soc.*, 2016, **138**, 15046–15056.
59 X. Ao, W. Zhang, Z. Li, J. G. Li, L. Soule, X. Huang, W. H. Chiang, H. M. Chen, C. Wang, M. Liu and X. C. Zeng, *ACS Nano*, 2019, **13**, 11853–11862.
60 Q. Yu, S. Lian, J. Li, R. Yu, S. Xi, J. Wu, D. Zhao, L. Mai and L. Zhou, *J. Mater. Chem. A*, 2020, **8**, 6076–6082.

61 S. Weon, D. Huang, K. Rigby, C. Chu, X. Wu and J. H. Kim, *ACS ES&T Engg*, 2021, **1**, 157–172.
62 Y. Tian, L. Xu, J. Qian, J. Bao, C. Yan, H. Li, H. Li and S. Zhang, *Carbon*, 2019, **146**, 763–771.
63 S. Zhang, Y. Gao, S. Cheng, Y. Yan, S. Zhang, G. Zhuang, S. Deng, Z. Wei, X. Zhong and J. Wang, *Catal. Sci. Technol.*, 2019, **9**, 97–105.
64 Q. Wang, Y. Lei, Z. Chen, N. Wu, Y. Wang, B. Wang and Y. Wang, *J. Mater. Chem. A*, 2018, **6**, 516–526.
65 S. Chen, L. Zhao, J. Ma, Y. Wang, L. Dai and J. Zhang, *Nano Energy*, 2019, **60**, 536–544.